Supporting Information:
Magnetic sensing with a self-assembled nanowire

N. Rossi,[1] B. Gross,[1] F. Dirnberger,[2] D. Bougeard,[2] and M. Poggio[1]

[1]*Department of Physics, University of Basel, 4056 Basel, Switzerland*

[2]*Institut für Experimentelle und Angewandte Physik,*
Universität Regensburg, D-93040 Regensburg, Germany

I. HOW CANTILEVER SIZE AFFECTS FORCE SENSITIVITY

A key component in any force microscopy is the force sensor. This device consists of a mechanical transducer, used to convert force into displacement, and an optical or electrical displacement detector. Although early atomic force microscopy (AFM) transducers were simply pieces of gold or aluminum foil [31], specially designed and mass-produced Si cantilevers soon became the industry standard and led to improved resolution and force sensitivity [32]. These micro-processed devices are now cheap, readily available, and designed – depending on the target application – to have integrated tips and a variety of other features including coatings, electrical contacts, or magnetic tips.

Conventional 'top-down' cantilevers are well-suited for the measurement of the large forces and force gradients present on the atomic-scale. Nevertheless, for some applications sensitivity to small forces is crucial. These range from mass detection, to cantilever magnetometry, to scanning measurements of friction forces, Kelvin probe microscopy, electric force microscopy, MFM, and force-detected magnetic resonance. This push towards higher sensitivity has generated an interest in using ever smaller mechanical forces transducers, especially those made by 'bottom-up' techniques. Researchers can now grow nanometer-scale structures such as carbon nanotubes (CNTs) and NWs with unprecedented mechanical properties. Unlike traditional cantilevers and other top-down structures, which are etched or milled out of a larger block of material, bottom-up structures are assembled unit-by-unit to be almost defect-free on the atomic-scale with perfectly terminated surfaces. This near perfection gives bottom-up structures a much smaller mechanical dissipation than their top-down counterparts.

The trend towards decreasing the size of mechanical transducers is based on fundamental principles. For a thermally limited mechanical force transducer, the fluctuation-dissipation theorem implies that the minimum detectable force and minimum detectable force derivative are limited by the force noise spectral density $S_F = 4k_BT\Gamma$, where k_B is the Boltzmann constant, T is the temperature, and Γ is the resonator's mechanical dissipation (friction coefficient). In particular, the transducer's force sensitivity is given by $F_{min} = \sqrt{4k_BT\Gamma}$. Note that $\Gamma = m\omega_0/Q$, where m is the motional mass of the mechanical resonator, ω_0 is its angular resonance frequnecy, and Q is its quality factor. In practice, this means that at a given temperature, a well-designed cantilever force transducer must simultaneously have

low $m\omega_0$ and large Q.

For a cylindrical cantilever (e.g. a NW) we can apply Euler-Bernoulli beam theory to relate its dimensions to force sensitivity. We find that $m\omega_0 \propto d^3/l$, where d is the diameter and l is its length. For sensitive transducers, experiments show that Q is limited by surface-related losses[1], which lead to a linear decrease of Q with increasing surface-to-volume ratio, i.e. $Q \propto d$. As a result, we see that $\Gamma \propto d^2/l$, meaning that long and thin cantilevers should be the most sensitive. In fact, a review of real transducers confirms this trend. Furthermore, if we fix the aspect ratio and scale each dimension of the cantilever uniformly by a factor β, we find that $\Gamma \propto \beta$ and therefore $F_{min} \propto \beta^{1/2}$. This implies that given a constant aspect ratio, smaller structures will be sensitive to smaller forces.

High mechanical resonance frequencies are also attractive for sensitive force transducers, since they allow for the measurement of fast dynamics and they decouple the sensor from common sources of noise. A prominent example is the additional noise experienced by a cantilever as its tip approaches a surface[2,3]. This so-called non-contact friction is largely due to electronic fluctuators on the surface and typically has a $1/f$-like frequency dependence. As a cantilever approaches a surface, Γ usually increases and its force resolution suffers. Such processes can be mitigated through the use of high-frequency cantilevers. When the resonant frequency of the mechanical oscillator is much higher than the characteristic frequency of the external noise, the resonator can be effectively decoupled from that noise. Since a cantilever's angular resonance frequency is given by $\omega_0 \propto d/l^2$, if we scale each dimension of the cantilever uniformly by β, we find $\omega_0 \propto 1/\beta$.

Therefore, in order to simultaneously maximize ω_0 and minimize F_{min}, the entire structure should be scaled down. This necessity for further reduction in cantilever size has positioned bottom-up techniques as the fabrication methods of the future.

II. OPTICAL SETUP FOR NANOWIRE MOTION DETECTION

The setup for the optical detection of the nanowire (NW) motion is entirely fiber-based. Fig. S1(a) shows its terminal part[4], which encases the fiber and the microscope lenses in a titanium frame to minimize mechanical drift as a function of temperature. Given the tiny amount of optical power interacting with the horizontal cross section of a NW ($\sim$ 200 nm), the use a high-NA focusing lens (as sketched in Fig. S1(b)) is desirable to keep the displacement detection as localized as possible along the NW. The tightly focused spot also maximizes the scattered light collection efficiency. The effective NA of the objective is 0.45 due to the slight mismatch in NAs between the fiber and the collimating lens.

The confocal arrangement of the lenses – with the fiber's mode field diameter (MFD) acting as a pinhole – allows for high imaging resolution and optical sectioning. In confocal microscopy, in fact, the final image is constructed by measuring an intensity for ev-

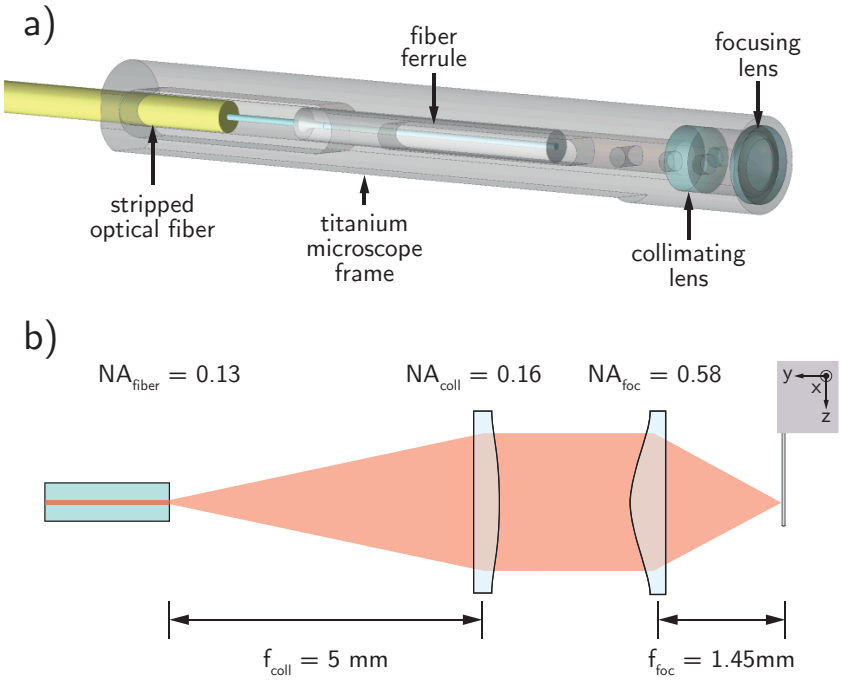

FIG. S1: Fiber-based confocal reflection microscopy setup and beam waist estimation. (a) 3D CAD microscope model. (b) Sketch of the optical setup. The lenses used are: *Thorlabs 354430-C* aspheric lens with an outer diameter of 2 mm and a clear aperture of 1.6 mm for beam collimation and *Thorlabs 354140-C* aspheric lens with an outer diameter of 2.4 mm and a clear aperture of 1.6 mm for focusing.

ery scanning position in the plane. The total coherent spread function (CSF) is given by $\mathrm{CSF}_{tot} = \mathrm{CSF}_{illum} \times \mathrm{CSF}_{det}$, where the former is determined by the field distribution of the focused excitation Gaussian beam and the latter by the spatial filtering properties of the pinhole (i.e. fiber's mode field) in the image plane[5].

A practical evaluation of the microscope's performance at a wavelength $\lambda = 1553\,\mathrm{nm}$ can be obtained by scanning the NW in the beam's waist area and collecting the reflected signal (see Fig. S2(a)). The obtained map shows interference fringes superimposed to a typical Gaussian waist profile. By taking a linecut along x at the focal plane (Fig S2(b)) – because of the sub-wavelength width of the NW along the scanning direction – it is possible to directly image the CSF_{tot} itself and fit it with a Gaussian curve. The profile of the beam incident on the NW, since in our case illumination and detection CSFs coincide, corresponds to $\mathrm{CSF}_{illum} = \sqrt{\mathrm{CSF}_{tot}}$ and has a waist $w_0 = 1.65\,\mu\mathrm{m}$ (see Fig. S2(c)). The measured waist is close to the theoretically calculated value of $1.52 \pm 0.15\,\mu\mathrm{m}$ for a polarization maintaining fiber with MFD $= 10.5 \pm 0.5\,\mu\mathrm{m}$. Deviations in the MFD and diffraction account for the slight magnification measured when defocusing with respect to the collimating lens.

As shown in Fig S2(d), the interferometer response can be treated as a simple two-component interference; multiple reflections in this low-finesse cavity can be neglected due to the poor reflectivity of the NW and fiber's cleaved facet[6]. The high visibility of the fringes allows for steep gradients and an extended linear region around quadrature (intensity I equal to its average value I_0) with a constant response at the NW motion on the order of few Vμm. By appropriately positioning the NW away from the optical axis, it is possible to probe the motion along arbitrary directions (set by the intensity gradient) at the expense of a decreasing sensitivity for angles progressively more orthogonal to the optical axis.

The choice of a standard communication wavelength and the relative low laser power of $25\,\mu\mathrm{W}$ allows us to neglect effects on the NWs' dynamics such as bolometric forces, radiation pressure, or changes in the Young modulus due to heating. This statement holds as long as the the focal spot is aligned several μm from MnAs particle at the end of the NW. When the focal spot overlaps with the MnAs tip, we observe heating up to $15\,\mathrm{K}$ in the displacement PSD of the two NW modes, due to absorption of light by the MnAs particle.

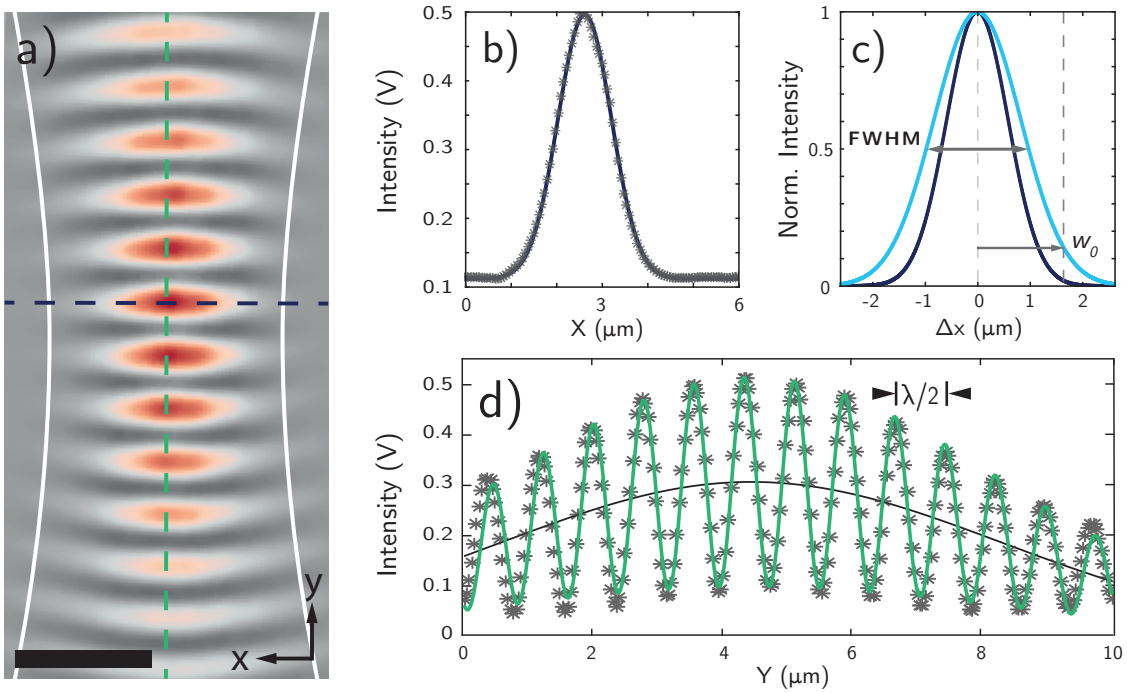

FIG. S2: Microscope characterization. (a) 2D map of the reflected light intensity as a function of NW position in the beam's waist (scale-bar 2 µm). The plot has been straightened by a rotation of 2.8°, indicating a small misalignment between the xy-scanners and the optical axis. (b) Intensity linecut along x at the focal plane (dashed blue line in (a)). Measured points (gray asterisks) are fit by a Gaussian curve with an offset given by the background noise (solid blue line). (c) Comparison between the CSF_{tot} (solid blue line) and the CSF_{illum} (solid cyan line). The CSF_{tot} is taken as the normalized fitted intensity profile in (b) and the CSF_{illum} as its squared root. The measured characteristics of the incident laser beam are a waist $w_0 = 1.65\,\mu\text{m}$ – at which the intensity drops by a factor of $1/e^2$ – and a full width at half maximum FWHM $= 2\,\mu\text{m}$. (d) Intensity linecut along the optical axis (dashed green line in (a)). The measured light intensity (gray asterisks) is fit (solid green line) as the response of a two-component interferometer $I = I_0(1 - V\cos(4\pi y/\lambda + \phi))$, where I_0 is the fit average Gaussian intensity (solid black line), $V = (I_{max} - I_{min})/(I_{max} + I_{min}) = 70\%$ is the fringe visibility, and wavelength $\lambda = 1553\,\text{nm}$. The most sensitive operating points are located at quadrature (i.e. where y is an odd multiple of $\lambda/8$) where the gradient is just given by $\partial I/\partial y = I_0 V 4\pi/\lambda$. In focus ($I_0$ is maximum), $\partial I/\partial y = 1.65\,\text{V}/\mu\text{m}$.

III. DISPLACEMENT CALIBRATION AND FORCE ESTIMATION

Scanning a NW sensor over a sample presents challenges and constraints, which are not present in pendulum AFM with conventional soft cantilevers. Practically, the scanned sample should not cut-off the beam's optical power upon approach of the NW nor modulate it while moving. At the same time, the profile of the first flexural mode (Fig S3(a)) requires that the amplitude of NW deflection reduces as one moves from its tip towards its clamping point. Given these two competing requirements, the working point on the NW has to be chosen far enough from the sample, but still with a good dynamic range for measuring its displacement.

In order to estimate the driving force from the mechanical response of each mode, it is crucial to know their amplitude of the motion r_i at the tip of the NW: given the first mode's normalized profile $u(z)$, plotted in Fig S3(a), this can be calculated as $r_i = r_i(z_{wp})u(z_{wp})^{-1}$ by measuring the distance of the working point from the tip z_{wp}.

In our setup, we can only finely position the NW with a limited scanning range of $\sim 2\,\mu\text{m}$ along the z-axis. Therefore, in order to crosscheck the value of z_{wp}, we estimate $u(z_{wp})$ by fitting the thermally driven displacement noise power spectral density (PSD) at the tip and at the working point, as shown in Fig S3(b). Both spectra are acquired projecting the modes' motion along the same measurement direction (i.e. optical gradient), coincident with the optical axis (i.e. y-axis).

Each PSD, acquired at an arbitrary position z along the NW, is fitted by the sum of the two independent Lorentian peaks:

$$\begin{aligned} S(\omega, z) &= (u(z))^2(S_1(\omega)\cos^2\theta_0 + S_2(\omega)\sin^2\theta_0) + S_n = \\ &= (u(z))^2 \frac{4k_BT}{m_e}\left(\frac{\omega_1}{Q_1}\frac{\cos^2\theta_0}{(\omega_1^2-\omega^2)^2+\left(\frac{\omega_1\omega}{Q_1}\right)^2} + \frac{\omega_2}{Q_2}\frac{\sin^2\theta_0}{(\omega_2^2-\omega^2)^2+\left(\frac{\omega_2\omega}{Q_2}\right)^2}\right) + S_n \end{aligned} \quad (1)$$

where θ_0 is the angle between $\hat{\mathbf{r}}_\mathbf{1}$ and $\hat{\mathbf{y}}$, S_n is the measurement noise floor and m_e is the effective mass of the resonator. It is important to point out that terms like Q_i, ω_i and θ_0 can be kept as fit parameters because of their independence, while T, m_e and $u(z)$ contribute to the overall scaling of the two Lorentians peaks and therefore only one of them can be set as fit parameter. By acquiring the thermal noise PSD in several positions along the NW as a function of the laser power, it is possible to figure out if T is greater than the

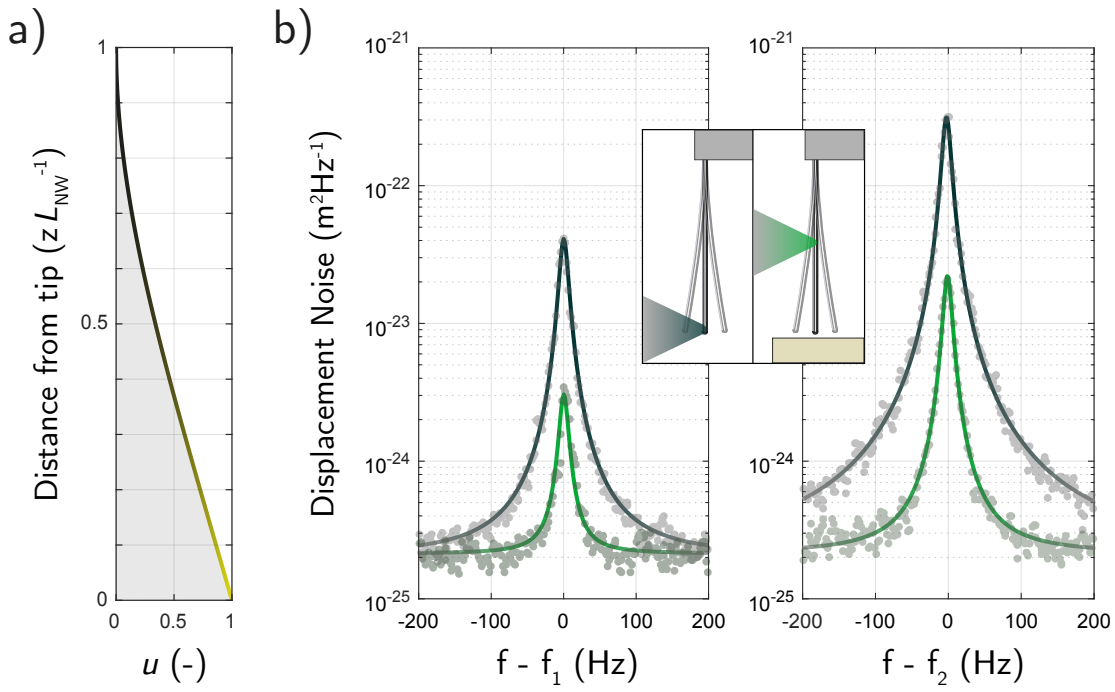

FIG. S3: Optical working point calibration for NW2. (a) First flexural mode shape function for singly-clamped nanowire of length L_{NW}. The function $u(z)$ is normalized to the maximum displacement value r_{tip}. (b) Zoomed plots around the two modes resonance frequencies $f_1 = 581$ kHz and $f_2 = 615$ kHz of thermally driven PSDs acquired at the tip and at the working point, as schematically shown in the inset. The raw spectral responses (gray dots) are fit by Eq 1: at the tip, $z \approx 0$, (dark gray solid line) the fit shows a slightly higher temperature $T = 7.5$ K , while at the working point $z = z_{wp}$, (green solid line) the fitted curve – for $T = 4.2$ K – returns a normalized mode displacement $u(z_{wp}) = 0.312$, which means that the scanning measurements were performed focusing the laser at a distance $z_{wp} = 0.52\, L_{NW} = 8.8\,\mu$m from the tip.

base temperature and if it is independent of z. Since m_e is constant and set only by the NW's geometry and material properties, a lowering of the resonant frequencies is usually a clear indication of heating. In our case, since we noticed an increase in temperature only for the laser illuminating the MnAs tip, we extracted m_e by fitting the measured power of each mode as a function of $(u(z))^2$ along the NW above the tip, where $T = 4.2$ K. The returned value of $m_e = 780$ fg is consistent - within 2% - with what expected from basic geometrical considerations and more accurate $COMSOL$ modeling of the NW structure and mode shape.

To summarize, the component of the force resonantly driving the mode i is calculated as $F_i = \frac{k_i}{Q_i} r_i = \frac{k_i}{Q_i} r_i(z_{wp}) u(z_{wp})^{-1}$, where $k_i = m_e \omega_i^2$ and $r_i(z_{wp})$ are obtained from the measured projected displacement signal x_{rms} as $r_1(z_{wp}) = x_{rms} \cos \theta_0{}^{-1}$ and $r_2(z_{wp}) = x_{rms} \sin \theta_0{}^{-1}$.

For the line scans, values of k_i and Q_i have been extracted from thermal noise spectra acquired at each point, but the difference from the intrinsic values is negligible because of the high value of Q_i compared to the shift $\Delta\omega_i$.

IV. MICROMAGNETIC SIMULATIONS FOR NW MAGNETOMETRY

The core of the simulation is the calculation of the magnetic energy of the MnAs tip for each value of the applied external field and for small tilt angles around the oscillation axis of each NW mode ($\hat{\mathbf{r}}_\mathbf{1}$,$\hat{\mathbf{r}}_\mathbf{2}$). To define the problem's geometry, we refer the hard axis direction (θ_K,ϕ_K) and every other possible misalignment to a principal reference system formed by the NW axis $\hat{\mathbf{n}}$ and the direction of the two modes of oscillation $\hat{\mathbf{r}}_\mathbf{i}$. More specifically, for each NW we take into account a small misalignment between $\hat{\mathbf{n}}$ and the external magnetic field $\mathbf{B}$ (θ_B,ϕ_B) as well as the orientation of the tip itself with respect to the NW (θ_t,ϕ_t) (see Table I below).

The deviation of the magnetic field with respect to the NW axis accounts for an imperfect perpendicular growth of each NW with respect to the substrate and for a small tilt angle of 2° along the optical axis $\hat{\mathbf{y}}$ of the NWs' chip holder. This design ensures that the NWs on the edge of the chip are the first objects to approach the bottom sample, avoiding any unwanted contact due to an imperfect parallelism between the two.

	(θ_K,ϕ_K)	(θ_B,ϕ_B)	(θ_t,ϕ_t)
NW1	(4.2°, 45.5°)	(2.5°, 160.5°)	(4.7°, 170°)
NW2	(8°, −9.5°)	(2.5°, 110.5°)	(0°, 0°)
NW3	(68.3°, 142.2°)	(5°, 137°)	(20°, 210°)

TABLE I: Summary of the angles giving the best fit to data for each NW.

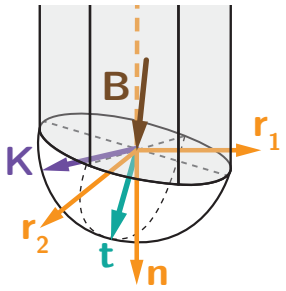

In the simulation for NW1, shown in Fig.2 (b,c) of the main text, the two pinning points are modeled in *Mumax3* by freezing the magnetization on a region of 4 cells ($\sim$ 10 nm × 10 nm) along the entire tip's height. In one case the magnetization is fixed along $-\hat{\mathbf{n}}$ and in the other along $+\hat{\mathbf{n}}$. The second pinning point on the vortex trajectory (see supplementary video) is not crucial for the evolution of the reversal process but counteracts – in terms of energy – the presence of the first one, preserving the symmetry of the frequency shift asymptotes for both the negative and positive high field limit.

In Fig. S4 and Fig. S5 we show the evolution of the simulated magnetization reversal for NW2 and NW3 respectively (see also supplementary videos).

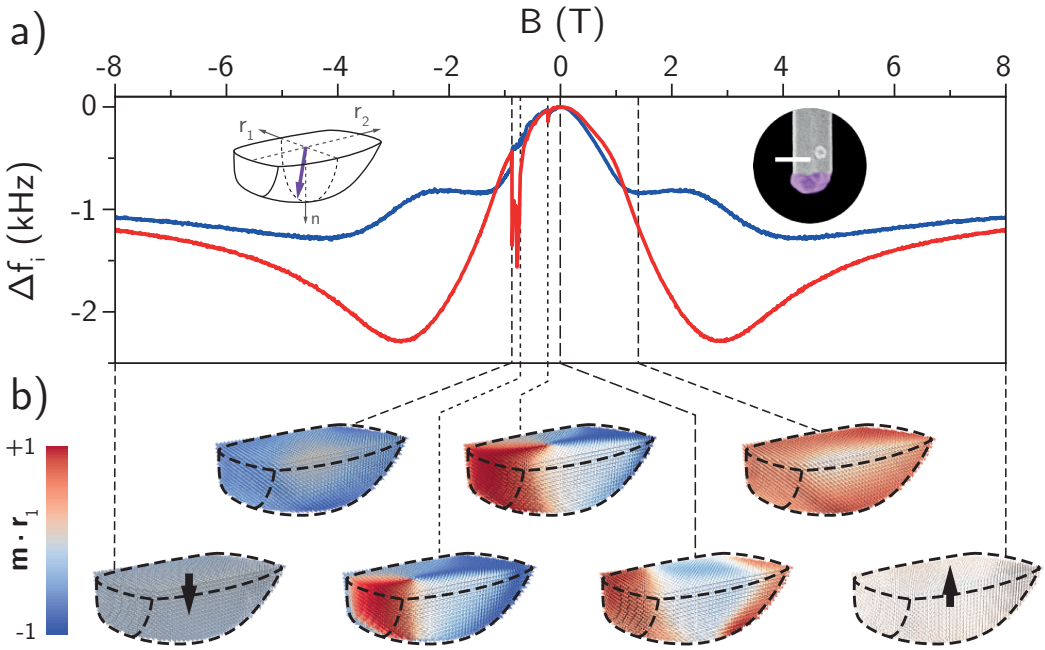

FIG. S4: NW2. (a) Calculated frequency shifts. Insets: sketch of simulated tip, SEM close up of NW2's tip (scale bar 200 nm). (b) Magnetization states for relevant values of B. Each cell is color-coded according to its magnetization component along $\hat{\mathbf{r}}_\mathbf{1}$.

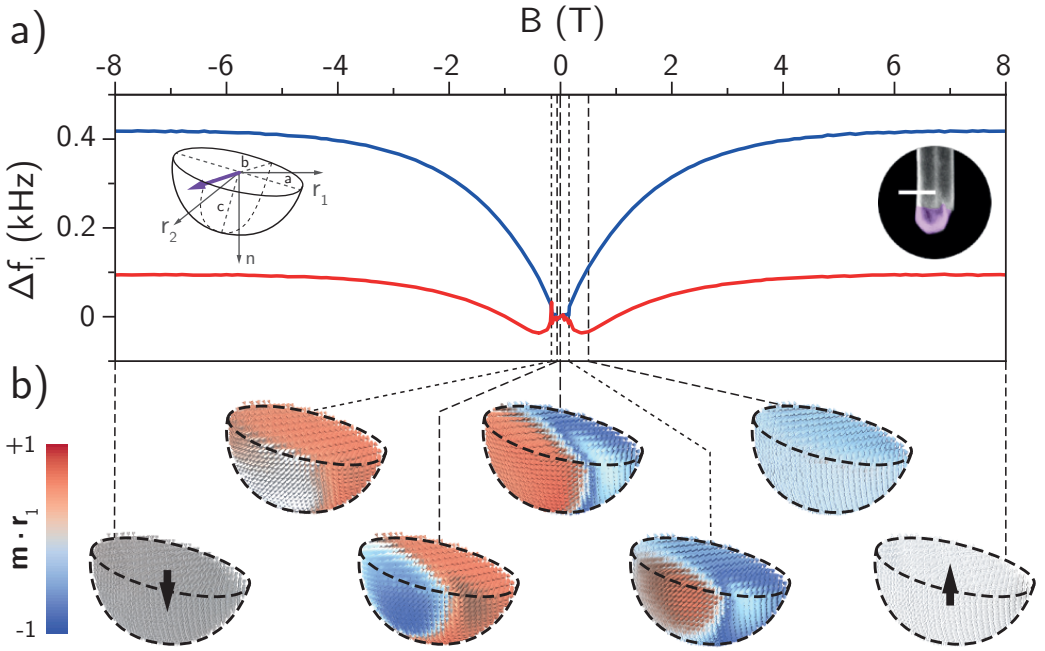

FIG. S5: NW3. (a) Calculated frequency shifts. Insets: sketch of simulated tip, SEM close up of NW3's tip (scale bar 200 nm). (b) Magnetization states for relevant values of B. Each cell is color-coded according to its magnetization component along $\hat{\mathbf{r}}_\mathbf{1}$.

V. SIMULATED MAGNETIC FIELD PROFILE $\mathbf{B_{AC}}$

In order to calibrate the NW magnetic response over the line scan, the monopole and dipole terms (q_0 and $\mathbf{m}$ respectively) are extracted from the complete driving force expression for each mode: $F_i = q_0 \mathbf{B}_{\mathrm{AC}} \cdot \hat{\mathbf{r}}_i + \nabla(\mathbf{m} \cdot \mathbf{B}_{\mathrm{AC}}) \cdot \hat{\mathbf{r}}_i + l_e^{-1}(\hat{\mathbf{n}} \times (\mathbf{m} \times \mathbf{B}_{\mathrm{AC}})) \cdot \hat{\mathbf{r}}_i$. The Biot-Savart field $\mathbf{B}_{\mathrm{AC}}$, generated by a current driven through the Au wire constriction at the modes' resonance frequencies, is calculated by the finite element simulation package *COMSOL*.

The (x,y) coordinates of the line scan with respect to the center of the wire are estimated by the direct imaging of the sample's topography[7]. Along $\hat{\mathbf{z}}$, the distance $d_z = 250$ nm between the wire and NW's tip is determined with a soft-touch onto the sample and consequent retraction by the desired amount with the z-axis piezo scanner (the absence of a direct calibration for this open-loop may introduce an error in the distance estimation around $\pm 10\%$).

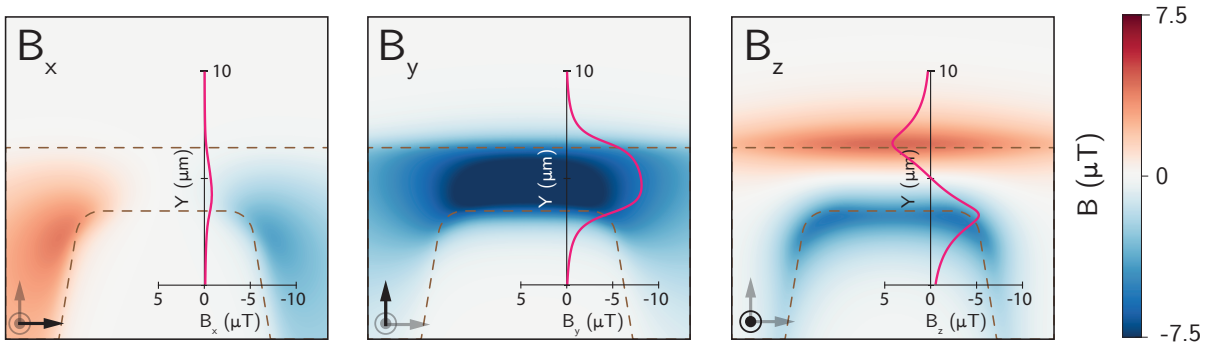

FIG. S6: Simulated magnetic stray field at a distance of 350 nm from the wire and for a current $I_{DC} = 50/\sqrt{2}$ µA flowing in $+x$ direction, used to fit the measured driving forces F_i for NW2. The field components are plotted separately over a 15 µm × 15 µm area centered above the Au wire constriction (dashed line contour). Each inset shows the value of the field component in correspondence of the acquired 10 µm-long line scan in $+y$ direction.

Given the µm-sized dimension of the wire and the modest frequencies around 500 kHz, the impedance of the wire is frequency independent, with a negligible reactive part; this fact allows us to approximate the problem with the static case where a DC current $I_{DC} = I_{AC}/\sqrt{2}$ flows through the wire. Following our point-probe approximation of the magnetic

tip behavior, the best fit with the data is obtained by taking the stray field calculated at a distance of 100 nm from the tip's apex (see Fig S6).

VI. SENSITIVITY TO DIFFERENT TYPES OF MAGNETIC FIELD SOURCES

In the experiments described in the main text, we find that our magnet-tipped NW has a thermally-limited displacement (force) sensitivity of 16 pm/$\sqrt{\text{Hz}}$ (4 aN/$\sqrt{\text{Hz}}$) at T = 4.2 K. Given the measured current transduction factor $\beta = 0.26\,\text{nm}/\mu\text{A}$ at the working distance $d_z = 250$ nm, we obtain a sensitivity to current flowing through our lithographically patterned wire of 63 nA/$\sqrt{\text{Hz}}$. Because of the dipole-like character of the MnAs tip, this transduction of current into displacement is dominated by the effect of the time-varying magnetic field gradient generated by the current at the position of the tip: $F_i \approx \nabla(\mathbf{m}\cdot\mathbf{B}_{\text{AC}})\cdot\hat{\mathbf{r}}_i = \mathbf{m}\cdot\nabla(\mathbf{B}_{\text{AC}}\cdot\hat{\mathbf{r}}_i)$. As discussed in the main text, the torque resulting from the time-varying magnetic field acting on the tip also produces an effective force, $T_i = l_e^{-1}(\hat{\mathbf{n}}\times(\mathbf{m}\times\mathbf{B}_{\text{AC}}))\cdot\hat{\mathbf{r}}_i$, but this term is typically secondary. Therefore, in the following analysis we restrict ourselves to considering the role of the magnetic field gradient. From *COMSOL* simulations of the field profile produced by current flowing through the wire, we find the measured current sensitivity to translate into a sensitivity to magnetic field gradient of $G_{\text{min}} = 11$ mT/(m$\sqrt{\text{Hz}}$) at the position of the tip's effective point probe, i.e. $d_z + d = 350$ nm above the surface.

As a result, in addition to knowing the sensitivity to the specifc current distribution flowing through our lithographically defined wire, we can now calculate the NW's sensitivity to other sources of magnetic field. We simply need to calculate the appropriate magnetic field gradient for each field source at the position of the probe and compare it to the demonstrated gradient sensitivity. For a tip with both its dipole moment and one of its modes oriented along $\hat{\mathbf{x}}$, the relevant component of the field gradient is $\hat{\mathbf{x}}\cdot\nabla(\mathbf{B}_{\text{AC}}\cdot\hat{\mathbf{x}}) = \partial B_{\text{AC},x}/\partial x$. Then, following a similar treatment by Kirtley[8] for magnetic scanning probes, we calculate the NW's expected sensitivity to a magnetic moment (dipole field), a superconducting vortex (monopole field), and an infinitely long and thin line of current (Biot-Savart field).

A magnetic moment $\mathbf{M}$ generates a magnetic field,

$$\mathbf{B}_M(\mathbf{r}) = \frac{\mu_0}{4\pi}\frac{3\hat{\mathbf{r}}(\hat{\mathbf{r}}\cdot\mathbf{M}) - \mathbf{M}}{r^3}, \tag{2}$$

where $\mathbf{r}$ is the distance from the moment to the position of the probe and μ_0 is the permeability of free space. If $\mathbf{M}$ is made to flip up and down along the $\hat{\mathbf{z}}$ direction, e.g. using magnetic resonance pulses as in magnetic resonance force microscopy[9], it generates a time-varying gradient, $\partial B_{\mathbf{M},x}/\partial x$. The amplitude of this gradient component is maximum directly above

or below the magnetic moment ($x = y = 0$) and has the following dependence on the vertical distance z:

$$\left(\frac{\partial B_{M,x}}{\partial x}\right)_{\max} = \frac{3\mu_0}{4\pi}\left(\frac{M}{z^4}\right). \tag{3}$$

We now take the maximum gradient component generated by a single electron, whose moment is given by the Bohr magneton μ_B. By comparing this term to our measured gradient sensitivity $G_{\min}$, we find a sensitivity to magnetic moment in terms of $\mu_B/\sqrt{\text{Hz}}$:

$$M_{\min} = G_{\min} \Big/ \left(\frac{\partial B_{\mu_B,x}}{\partial x}\right)_{\max} = \frac{4\pi}{3\mu_0}\left(\frac{G_{\min}}{\mu_B}\right) z^4. \tag{4}$$

If we assume the same tip-sample spacing as in our measurements of current flowing through our lithographically patterned wire, $z = d_z + d = 350$ nm, we find $M_{\min} = 50\ \mu_B/\sqrt{\text{Hz}}$.

We can carry through a similar procedure for the sensitivity to a superconducting vortex, modeled as a magnetic monopole generating a field,

$$\mathbf{B}_{\Phi_0}(\mathbf{r}) = \frac{\Phi_0}{2\pi r^2}\hat{\mathbf{r}}, \tag{5}$$

where $\mathbf{r}$ is the distance from the vortex to the position of the probe and $\Phi_0 = h/(2e)$ is the magnetic flux quantum. If the position of this vortex is modulated, it will generate a time-varying gradient, $\partial B_{\Phi_0,x}/\partial x$. As before, the amplitude of this component is maximum directly above or below the vortex ($x = y = 0$) and has the following dependence on the vertical distance z:

$$\left(\frac{\partial B_{\Phi_0,x}}{\partial x}\right)_{\max} = \frac{\Phi_0}{2\pi}\left(\frac{1}{z^3}\right). \tag{6}$$

The sensitivity to magnetic flux in terms of $\Phi_0/\sqrt{\text{Hz}}$ is then given by,

$$\Phi_{\min} = G_{\min} \Big/ \left(\frac{\partial B_{\Phi_0,x}}{\partial x}\right)_{\max} = 2\pi\left(\frac{G_{\min}}{\Phi_0}\right) z^3. \tag{7}$$

Again, by assuming the same tip-sample spacing as in our measurements, $z = d_z + d = 350$ nm, we find $\Phi_{\min} = 1\ \mu\Phi_0/\sqrt{\text{Hz}}$.

Finally, we calculate the expected sensitivity to an infinite line of current $\mathbf{I}$ generating a field,

$$\mathbf{B}_I(\mathbf{r}) = \frac{\mu_0}{2\pi}\frac{\mathbf{I}\times\hat{\mathbf{r}}}{|\hat{\mathbf{I}}\times\mathbf{r}|}, \tag{8}$$

where $\mathbf{r}$ is the distance from the current line to the probe position and $\mathbf{I} \parallel \hat{\mathbf{y}}$. By modulating I, one can generate a time-varying gradient, $\partial B_{I,x}/\partial x$. The amplitude of this component

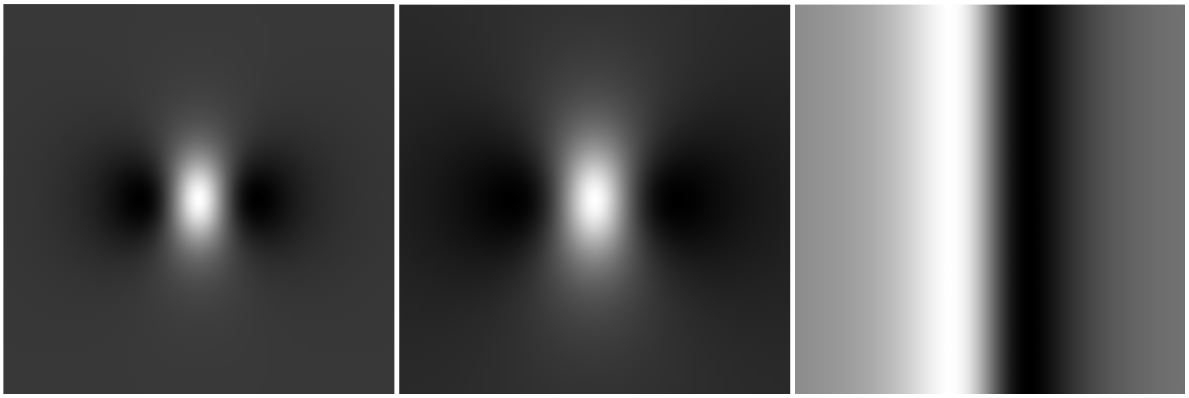

FIG. S7: Magnetic field gradients due to different sources plotted in the xy-plane. Left: $\partial B_{\mathbf{M},x}/\partial x$ resulting from a single electron at the origin with moment $\mu_B\hat{\mathbf{z}}$. Middle: $\partial B_{\Phi_0,x}/\partial x$ resulting from a single superconducting vortex at the origin. Right: $\partial B_{I,x}/\partial x$ for $I = 1$ A of current flowing through an infinitely long and thin wire along $\hat{\mathbf{y}}$. All plots show the gradients components in gray-scale in the $z = 350$ nm plane over a range of $2\,\mu\text{m} \times 2\,\mu\text{m}$.

is maximum in the planes defined by $x = \pm z/\sqrt{3}$. In those planes, I produces a maximum gradient amplitude with the following dependence on z:

$$\left(\frac{\partial B_{I,x}}{\partial x}\right)_{\text{max}} = \frac{3\sqrt{3}\mu_0}{16\pi}\left(\frac{I}{z^2}\right). \tag{9}$$

The resulting sensitivity to a line of infinite current in terms of $\text{A}/\sqrt{\text{Hz}}$ is given by,

$$I_{\text{min}} = G_{\text{min}} \Big/ \left(\frac{\partial B_{I,x}}{\partial x}\right)_{\text{max}} = \frac{16\pi}{3\sqrt{3}\mu_0}\left(\frac{G_{\text{min}}}{I}\right) z^2, \tag{10}$$

where $I = 1$ A. Assuming the same tip-sample spacing as in our measurements, $z = d_z + d = 350$ nm, we find $I_{\text{min}} = 9\ \text{nA}/\sqrt{\text{Hz}}$. Note the better sensitivity of the NW to an infinitely long and thin line of current than to the test currents of our experiments, which are distributed across a wider wire.

It is interesting to note the different scaling exponents of the tip-sample spacing in the expressions for the sensitivity to the difference field sources. The magentic moment, superconducting vortex, and current line sensitivity scale with the 4^{th}, 3^{rd}, and 2^{nd} power of z, respectively. In particular, sensitivity to magnetic moment could be greatly improved by smaller tip-sample spacing. The gain in the magnetic field gradient (proportional to z^{-4}) should more than compensate for the reduction of the effective tip moment interacting with the sample moment (roughly proportional to z^3).

[1] Y. Tao, P. Navaretti, R. Hauert, U. Grob, M. Poggio, and C. L. Degen, Nanotechnology **26**, 465501 (2015), ISSN 0957-4484.

[2] B. C. Stipe, H. J. Mamin, T. D. Stowe, T. W. Kenny, and D. Rugar, Phys. Rev. Lett. **87**, 096801 (2001).

[3] S. Kuehn, R. F. Loring, and J. A. Marohn, Phys. Rev. Lett. **96**, 156103 (2006).

[4] A. Högele, S. Seidl, M. Kroner, K. Karrai, C. Schulhauser, O. Sqalli, J. Scrimgeour, and R. J. Warburton, Review of Scientific Instruments **79**, 023709 (2008), ISSN 0034-6748, URL https://aip.scitation.org/doi/abs/10.1063/1.2885681.

[5] L. Novotny and B. Hecht, in *Principles of Nano-Optics* (Cambridge University Press, 2006), pp. 89–133.

[6] D. Rugar, Applied Physics Letters **55**, 2588 (1989), ISSN 0003-6951, URL http://aip.scitation.org/doi/10.1063/1.101987.

[7] N. Rossi, F. R. Braakman, D. Cadeddu, D. Vasyukov, G. Tütüncüoglu, A. Fontcuberta i Morral, and M. Poggio, Nat. Nanotechnol. **12**, 150 (2017).

[8] J. R. Kirtley, Rep. Prog. Phys. **73**, 126501 (2010).

[9] M. Poggio and B. E. Herzog, in *Micro and Nano Scale NMR* (Wiley-Blackwell, 2018), pp. 381–420, ISBN 978-3-527-69728-1.